Chemical Science

ROYAL SOCIETY OF CHEMISTRY

EDGE ARTICLE

View Article Online
View Journal | View Issue

Open Access Article. Published on 30 April 2025. Downloaded on 3/29/2026 5:07:54 PM.
This article is licensed under a Creative Commons Attribution-NonCommercial 3.0 Unported Licence.

Check for updates

Cite this: *Chem. Sci.*, 2025, **16**, 9501

All publication charges for this article have been paid for by the Royal Society of Chemistry

Simultaneous electron and proton conduction in a stable metal organic material with highly selective electrocatalytic oxygen reduction reaction to water†

Rajat Saha,*[a] Amitosh Sharma,[b] Anjila I. Siddiqui,[c] Samia Benmansour,[a] Joaquín Ortega-Castro,[d] Antonio Frontera,[d] Biswajit Mondal,*[c] Myoung Soo Lah*[b] and Carlos J. Gómez García*[a]

Proton coupled electron transfer (PCET) is considered as the elementary step of several chemical, electrochemical and biological processes and thus the development of dual conducting materials has recently become a major focus in Chemical Science. Herein, we report the highly selective electrocatalytic oxygen reduction to water by the stable dual conducting metal–organic material (MOM) $[Cu(INA)_2(H_2O)_4]$ (INA = isonicotinate). Structural analysis reveals the important role of both, hydrogen bonding and π-interactions, in the formation of a supramolecular 3D network. Theoretical calculations show that hydrogen bonding interactions among the coordinated water molecules and deprotonated carboxylate oxygen atoms induce proton transport ($2.26 \pm 0.10 \times 10^{-5}$ S cm^{-1} at 98% RH) while weak intermolecular π-interactions (π–π and anion–π) provide the pathway for electron transport ($1.4 \pm 0.1 \times 10^{-7}$ S cm^{-1} at 400 K). Such dual proton and electron conductivity leads to a selective oxygen reduction reaction (ORR) to water in an alkaline medium. To the best of our knowledge, this is the first report on electrocatalytic ORR by a dual-conducting metal–organic material.

Received 2nd April 2025
Accepted 20th April 2025

DOI: 10.1039/d5sc02474a

rsc.li/chemical-science

Introduction

The prediction of the implications of multiple proton/electron transfer reactions for electrocatalysis[1] and the recent achievement of PCET has recently rushed the development of dual-conducting "ionoelectronic" materials.[2] Several biological processes (photosynthesis, respiration, enzymatic reactions, *etc.*) chemical energy devices (fuel cells, solar cells, *etc.*) and electrochemical reactions (electrocatalytic CO_2 reduction, nitrogen reduction, oxygen reduction reaction (ORR) and water splitting) rely on the transfer of both, protons and electrons. Both charge carriers, protons and electrons, may originate from one or from different materials, may transfer in one or different directions and may take place either sequentially or concertedly.[3,4] Some processes even involve multiple electron and proton transfer. Therefore, the design of dual-conducting materials able to conduct both, electrons and ions (protons), simultaneously has become a prime focus of research for their energy and environment related applications.[5–7] Traditional dual conducting materials are prepared by physical blending of individual electron and proton conductors.[8] Such physical mixing leads to the formation of uncontrollable and inefficient conducting pathways which ultimately results in poor performance.[9] Some graphene oxides and perovskites have shown better conducting properties but the lack of detailed structural information hinders further systematic development.[10,11] Therefore, the synthesis and fully characterization of dual conducting materials for its implementation in practical applications and further development, remains a challenge.

Crystalline metal–organic materials[12] (MOMs) are well-known for their regular periodic and tuneable structures and useful functionalities like adsorption, storage, catalysis, *etc.* In the last decade, there has been an increasing interest in the design of electron[13] and proton conducting[14] MOMs. Different strategies like the use of soft donor-based ligands, redox active metal ions and ligands, encapsulation of electroactive cations, molecules or conducting polymers, *etc.* have been used to design electrically conducting MOMs for their possible applications in electrocatalysis, chemresistive sensing, *etc.*[15] Proton donor and acceptors as H_2O, –COOH, $-SO_3H$, *etc.*, can be

[a]*Departamento de Química Inorgánica, Universidad de Valencia, Dr Moliner 50, Burjasot, Valencia, 46100, Spain. E-mail: carlos.gomez@uv.es; rajat.saha@uv.es*
[b]*Department of Chemistry, Ulsan National Institute of Science and Technology, Ulsan, 44919, Republic of Korea*
[c]*Discipline of Chemistry, IIT Gandhinagar, Palaj, 382355, Gujarat, India*
[d]*Departament de Química, Universitat de les Illes Balears, Crta de Valldemossa km 7.5, Palma de Mallorca, 07122, Baleares, Spain*

† Electronic supplementary information (ESI) available. CCDC 2369691. For ESI and crystallographic data in CIF or other electronic format see DOI: https://doi.org/10.1039/d5sc02474a

Open Access Article. Published on 30 April 2025. Downloaded on 3/29/2026 5:07:54 PM. This article is licensed under a Creative Commons Attribution-NonCommercial 3.0 Unported Licence.

introduced within the MOMs (either connected to the metal ions, as functional groups in the ligands or as guests in the void space) to develop proton-conducting materials for their use in proton exchange membrane fuel cells (PEMFCs).[16] The development of a MOM with dual electron and proton conductivity is, therefore, an interesting challenge that has only been achieved recently is a few cases. One of these examples was prepared by Su *et al.* who have shown the pseudo-capacitive behaviour of a dual-conducting 2D metalorganic framework (MOF), where proton transport occurs through guest dimethylammonium cations and electron transport relies on the redox-active tetrathiafulvalene moiety.[17] Another interesting example was reported by Zou *et al.* for a Ag-based coordination polymer with a triazole based ligand that shows electrocatalytic CO_2 reduction.[18]

Donashita *et al.* have very recently developed a dual conducting molecular material by encapsulating a redox-active tetrathiafulvalene moiety within the supramolecular channels of $[Pt_2(pmdt)_4]$ (where pmdt = phosphonomethane dithiolate).[19] The hydrogen bonding motifs of the paddle wheel moieties generate proton conducting pathways while electron conduction takes place through multiple charge transfer interactions. Very recently, He *et al.* have showed a nice example of modulation of the dual conducting behaviour of a 2D MOF through intercalation of 2D inorganic layers.[20] A similar modulation has also been very recently reported by Choi *et al.* in a 2D MOF by replacing coordinated water with urea.[21]

Despite their many possibilities, based on their unique properties, there are very few reported examples of dual conductors and all of them have been reported in the last five years (Table S1†).[17–26] It is, therefore, very important to develop and characterize new dual conducting well-structured materials to understand their conducting mechanisms and pathways for their possible applications.

Oxygen reduction reaction (ORR) is one of the key processes in fuel cell technology and is of significant interest in electrocatalysis.[27] In ORR, molecular O_2 is electrochemically reduced by four electrons and four protons into water or by two electrons and two protons into hydrogen peroxide.[28] The efficiency of PEMFC is also dependent on the catalytic conversion of oxygen to water at the cathode surface while protons are transported from the anode through the proton exchange membrane.[29] Thus, the design of suitable ORR electrocatalysts has become a major challenge in both academic and industrial research. The design of a catalyst that can supply both, protons and electrons, is considered as a paramount challenge to develop this technology.[30,31] Thus, Xu *et al.* have recently theoretically predicted the enhancement of the electrocatalytic ORR activity with proton conducting 1D coordination polymers.[32] Barile *et al.* have shown that it is possible to tune the electrocatalytic ORR activity of a molecular catalyst by controlling the proton transfer (with a lipid membrane modified with proton carriers) and the electron transport (with thiol-based self-assembled monolayers on gold electrodes).[30] Furthermore, there are some reports showing an enhancement of the catalytic activity with the help of proton conducting MOFs, as those of Zhang *et al.* showing an increase of the electrocatalytic oxygen evolution reaction (OER) activity with increasing the proton conductivity[33] and Schroder *et al.*, who have reported photocatalytic hydrogen evolution reaction (HER) with a proton-conducting MOF.[34] Nevertheless, in none of these examples, the catalyst is the electron and proton conductor and, as far as we know, there is no evidence of electrocatalytic ORR activity using a material that shows simultaneous proton and electron transport.

In this context, we have attempted to explore the dual conducting behaviour of a metal–organic material for the possible applications in ORR activity. For this, we have chosen the supramolecular complex $[Cu(INA)_2(H_2O)_4]_n$ (where INA = isonicotinate), that self-assembles *via* both supramolecular hydrogen bonding and π-interactions in the solid state. Note that, although the structure of this compound has already been published several times, along with its capacity to absorb some dyes,[35–42] there are no studies on its electrical and proton conductivity nor its ORR to water. Here we show the dual proton and electron conductivities and a high activity and selectivity for the electrocatalytic oxygen reduction to water displayed by this compound. We also present its magnetic characterization and the theoretical calculations to show the electron and proton mechanisms.

Results and discussion

Structure of $[Cu(INA)_2(H_2O)_4]$ (1)

Since the structure of compound **1** has already been described (Table S2†),[35–42] here we will focus on the key intermolecular interactions (H-bonds and π-interactions) responsible for the electronic and proton conductivity observed in this compound.

Compound $[Cu(INA)_2(H_2O)_4]$ (**1**) consists of a centrosymmetric monomer with an octahedral Cu^{II} atom connected to two *trans* water molecules and two *trans* isonicotinate anions in the equatorial plane and two water molecules in the axial positions. As expected, the axial Cu–O bond distance (2.417(2) Å) is much longer than the equatorial Cu–O and Cu–N ones (1.9922(19) and 2.007(2) Å, respectively, Table S3†), due to the expected Jahn–Teller distortion (Fig. S1†). The monomers pack in the solid state to form 3D supramolecular assemblies by a combination of hydrogen bonds (Fig. S2–S5 and Table S4†) and π–π and π–anion stacking interactions (Fig. S6 and Table S5†). These interactions play a crucial role in stabilizing the solid state structure of the supramolecular complex **1**, as depicted in Fig. 1a. These H bonds are formed between the coordinated water molecules, that act as strong H-bond donors, and the carboxylate anions, that serve as excellent H-bond acceptors.

Additionally, antiparallel π-stacking is favoured due to the antiparallel orientation of local dipoles, which are notably strong owing to the zwitterionic nature of the complex and its charge separation. A detailed view of the H-bonds contributing to the 2D assembly is provided in Fig. 1b. Notably, four water molecules and two carboxylate groups from four distinct complexes interact, forming six charge-assisted H-bonds (Fig. S2†). Two water molecules act as bridges linking two carboxylates each, while each of the other two water molecules form a single H-bond (Fig. 1b). Hydrogen atoms not involved in the H-bonding network of the 2D assembly are highlighted in

 © 2025 The Author(s). Published by the Royal Society of Chemistry

Open Access Article. Published on 30 April 2025. Downloaded on 3/29/2026 5:07:54 PM.
This article is licensed under a Creative Commons Attribution-NonCommercial 3.0 Unported Licence.

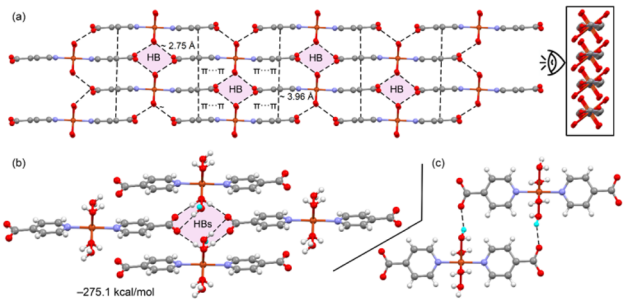

Fig. 1 (a) Partial view of the crystal structure of **1**, showing H-bonds and π−π stacking. (b) Detail of the tetrameric unit of compound **1** with indication of the H-bonds, differentiating the two different types of water. (c) Dimeric assembly to represent how the planes are interconnected.

blue in Fig. 1b and c. These atoms help to link the 2D assemblies to generate the final 3D architecture (Fig. S3–S5†). Details of the H-bonds that connect the 2D assemblies are shown in Fig. 1c and the structural parameters of these bonds are listed in Table S4.† The pyridyl rings of the INA ligands are engaged in face-to-face π···π interactions (purples lines in Fig. S6†) (centroid–centroid distance = 3.9659(15) Å) (Table S5†) and in anion–π interactions established with the carboxylate oxygen atoms (green lines in Fig. S6,† O-centroid distance = 3.430(2) Å, Table S5†). These π···π and anion–π interactions generate 2D supramolecular lattices parallel to the crystallographic *bc* plane (Fig. S6†). Hirshfeld surface analysis and the corresponding 2D fingerprint plots clearly indicate that the hydrogen bonding interactions, π···π and anion–π interactions contribute 21.1, 10.0 and 2.7%, respectively, to the overall Hirshfeld surface of the structure (Fig. S7 and S8†).

The calculated formation energy of the tetrameric assembly depicted in Fig. 1b is remarkably large (−275.1 kcal mol^{-1}). A detailed description of the reasons explaining this high energy can be found in the ESI and in Fig. S9.†

Physicochemical characterization of $[Cu(INA)_2(H_2O)_4]$ (1)

Compound **1** shows a high stability in water over the pH range 3–14 for more than 24 h but it is unstable below pH = 3. The powder X-ray diffraction (PXRD) pattern of **1** (Fig. S10†) shows the appearance of new peaks for the sample soaked in an aqueous HCl solution at pH = 1 but the PXRD patterns are identical in the pH range 3–14. This observation is also confirmed by the UV-vis (Fig. S11†) and IR spectra (Fig. S12 and S13†). An aqueous suspension of **1** shows one intense band at 268 nm that remains unaltered in the pH range 3–14 whereas two new bands appear at 262 and 212 nm for pH ≤ 2. Similarly, IR spectra show that at pH = 1 the bands at 1506 cm^{-1} and 1522 cm^{-1}, corresponding to the free carboxylate groups, disappear and a new band appears at 1587 cm^{-1}. PXRD also shows high stability in different solvents as *N*,*N*′-dimethylformamide, methanol, acetonitrile, *etc.* as well as in boiling water (Fig. S10 and S14†).

Energy dispersive X-ray spectroscopy studies and elemental mapping (Fig. S15–S17†) also confirm the composition of the material. Thermogravimetric analysis reveals that the material loses its coordinated water molecules within the temperature range 120–160 °C (theoretical = 18.95%; experimental = 19.00%, Fig. S18†). Variable temperature PXRD indicates that the material is stable up to 110 °C (Fig. S19†).

Solvent adsorption studies have been done for compound **1** after activation by heating at 80 °C for 4 h under vacuum. The activated material shows irreversible water adsorption behaviour with a high hysteresis (Fig. S20†). The sorption profile indicates that the activated material starts to adsorb water at very low pressure and there is a sudden increase in adsorption at 65% relative humidity (RH) and almost completed at 90% RH while the desorption curve shows almost 100% retention even at 0% RH with a large hysteresis (Fig. S20†). The PXRD pattern after adsorption shows that there is no change in the structure of the material after the water sorption study (Fig. S21†). This result indicates that the material losses all its four coordinated water molecules at 80 °C under vacuum during activation and adsorbs them within a RH range of 65–90%.

Given the presence of intermolecular interactions, we have studied the influence of these weak interactions on the magnetic properties of compound **1**. The variable temperature magnetic study shows that this material presents a weak antiferromagnetic interaction. The room temperature $\chi_m T$ value is 0.4 cm^3 K mol^{-1} (χ_m is the molar magnetic susceptibility per Cu^{II} ion) and it remains almost constant down to 30 K. Below this temperature $\chi_m T$ decreases and reaches a value of 0.25 cm^3 K mol^{-1} at 2 K (Fig. S22†). The magnetic data have been fitted to the regular $S = \frac{1}{2}$ chain model proposed by Hatfield *et al.*[43] with a Hamiltonian of the type $H = -J[S_i S_{i+1}]$. This model reproduces very satisfactorily the magnetic data of compound **1** in the whole temperature range with g = 2.0814(4) and J = −1.62(1) cm^{-1} (solid line in Fig. S22†). This behaviour confirms the presence of a weak antiferromagnetic Cu···Cu coupling that can be attributed to the presence of both the π–π stacking and the H-bonds along the crystallographic *b*-axis (Fig. S23†). The weak antiferromagnetic coupling is similar to those observed for other Cu^{II} compounds with similar intermolecular interactions through H-bonds and π–π stacking.[44,45]

Theoretical prediction on dual conductivity in the supramolecular complex $[Cu(INA)_2(H_2O)_4]$ (1)

The molecular electrostatic potential (MEP) surface of **1** has been calculated and is depicted in Fig. 2a. The MEP values at the water protons are notably high, ranging from 97.3 kcal mol^{-1} for the water molecule acting as a bridge to 89.1 kcal mol^{-1} for the water molecule that connects the supramolecular planes. As expected, the MEP minimum is found at the oxygen atoms of the carboxylate groups, registering at −74.0 kcal mol^{-1}. These extreme MEP values at both minimum and maximum are indicative of the formation of very strong hydrogen bonds and support the observed proton mobility within this compound.

Additionally, the MEP on the aromatic rings is significantly large and positive, which facilitates the antiparallel orientation and substantial displacement observed in the π-stacking interactions. Here, the negatively charged carboxylate group is

Open Access Article. Published on 30 April 2025. Downloaded on 3/29/2026 5:07:54 PM.
This article is licensed under a Creative Commons Attribution-NonCommercial 3.0 Unported Licence.

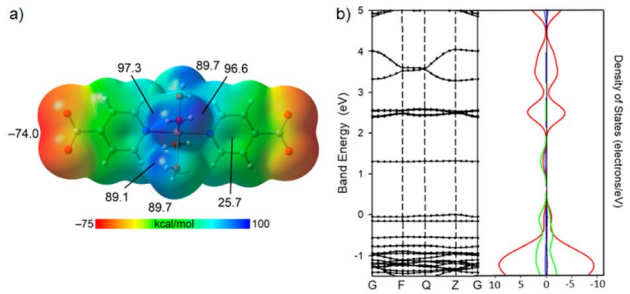

Fig. 2 (a) MEP surface of MOM **1** with the MEP values at selected points of the surface. (b) Electronic band structure and partial alpha (left) and beta (right) density of states of MOM **1**. Points of high symmetry in the first Brillouin zone are labelled as follows: $G = (0, 0, 0)$, $F = (0, 0.5, 0)$, $Q = (0, 0.5, 0.5)$ $Z = (0, 0, 0.5)$. The s, p and d-states are shown as blue, red and green lines, respectively.

positioned over the positively charged pyridine ring, contributing to the stability of the structure through electrostatic complementarity. Following such electrostatic interaction, we have calculated the band structure of MOM **1** to predict its electrical response (Fig. 2b). According to the band diagram and the partial density of states diagram (PDOS), the crystal exhibits semiconductor properties. In the conduction region (0 to 5.0 eV), three areas with well-defined energy levels are identified. The level closest to the valence zone is located at 1.32 eV and is primarily influenced by the copper's d orbitals. This level shows only a population of alpha electrons, as observed in the PDOS, suggesting low occupancy. The next band set, with a separation between 2.41 and 2.56 eV from the valence band, corresponds to p-type orbitals of the pyridine molecule in the crystal. Finally, another group of bands dispersed between 3.28 and 4.00 eV also shows a predominance of p-orbital character. In the valence zone, the levels closest to 0 eV, taken as a reference for the Fermi level, are associated with the d-type orbitals of copper atoms, exhibiting slightly different densities of alpha and beta electrons. This behaviour highlights the crucial role of copper in the electronic properties of the material.

We have also calculated the material ability to polarize in response to an electric field and the loss of energy (often as heat) under an applied electric field. The analysis was performed in the crystal's three directions (*xx*, *yy*, *zz*), revealing markedly different behaviours (Fig. S24†). We observe how the dielectric function begins to increase, reaching a small maximum around 2.5 eV, with a significant increase when photons with energies above approximately 3 eV are irradiated and this behaviour is consistent in all crystal directions though there is a significant decrease in the *yy* direction that houses the pyridine rings arranged almost perpendicular to the propagation direction.

Additionally, we have also examined the electron distribution within the unit cell through the electron localization function (ELF) (Fig. S25†). The analysis of the ELF iso-surfaces shows the presence of zones with elevated ELF values that align with regions of intermolecular interactions, such as anion–π interactions. This fact likely contributes to the moderate electrical conductivity observed in MOM **1**, providing insights into the electron dynamics that influence its electrical properties.

Proton conductivity in MOM $[Cu(INA)_2(H_2O)_4]$ (1)

The free carboxylate moieties and coordinated water molecules within the framework form a 3D hydrogen-bonded network (Fig. S2–S5†) which facilitates the proton transport. Hence, we have studied the proton transport efficiency of the supramolecular complex **1** with alternating current (AC) electrochemical impedance spectroscopy (EIS) on pelletized samples. As already indicated, the four coordinated water molecules play a crucial role in the formation of the hydrogen-bonded network. Additionally, the water sorption behaviour of the fully activated MOM **1** shows that the water molecules coordinate to the metal ion when the relative humidity increases, reaching saturation for four coordinated water molecules as shown by the weight gain (experimental = 24.50%, calculated = 23.41% for RH above 90%, Fig. S18†). Consequently, the activated MOM **1** is expected to show humidity-dependent proton conductivity due to the different hydrogen bonded pathways based on the amount of coordinated water. The experimental results confirm this assumption. Thus MOM **1** shows an increase in the proton conductivity value with increasing the RH at 25 °C with values at 60, 70, 80, 90 and 98% RH of $2.06 \pm 0.09 \times 10^{-10}$, $6.10 \pm 0.26 \times 10^{-9}$, $1.20 \pm 0.05 \times 10^{-7}$, $1.23 \pm 0.05 \times 10^{-6}$ and $2.26 \pm 0.10 \times 10^{-5}$ S cm^{-1}, respectively (Fig. S26 and Table S6†). The stability of the supramolecular complex **1** has also been confirmed after the proton conductivity measurements (Fig. S27†).

The dependence of the proton conductivity with temperature was also monitored by keeping RH constant at 98% and increasing the temperature from 25 to 75 °C. MOM **1** shows a continuous increment of the proton conductivity with increasing temperature in the range 25–75 °C (Fig. 3a).

The highest proton conductivity at 75 °C is $4.14 \pm 0.18 \times 10^{-5}$ S cm^{-1}. Such high proton conductivity without any acidic moiety has to be attributed to the 3D hydrogen-bonded array formed by the free carboxylate groups and the coordinated water molecules. One of the key features for optimum fuel cell is a low activation energy so that power density of the fuel cell can be maintained in a wide range of temperatures. The activation energy for the proton transport over the temperature range 25–75 °C with 98% RH has been calculated with the Arrhenius plot for MOM **1** (Fig. 3b). This plot shows a low activation energy of

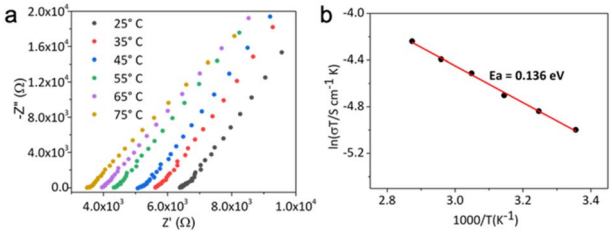

Fig. 3 (a) Nyquist plots of a pellet of MOM **1** at 98% RH and different temperatures in the range 25–75 °C. (b) Arrhenius plot of the proton conductivity of **1** at 98% RH in the temperature range 25–75 °C.

 © 2025 The Author(s). Published by the Royal Society of Chemistry

Open Access Article. Published on 30 April 2025. Downloaded on 3/29/2026 5:07:54 PM.
This article is licensed under a Creative Commons Attribution-NonCommercial 3.0 Unported Licence.

0.136 eV, demonstrating that the proton transport follows the Grotthuss mechanism with proton hopping.[46,47]

Electrical conductivity in MOM $[Cu(INA)_2(H_2O)_4]$ (1)

The solid state electronic absorption spectrum of MOM **1**, shows an optical bandgap of ~2.62 eV at room temperature (Fig. S28a†) due to intermolecular π-interactions close to the value gap obtained with the Tauc plot (2.87 eV, Fig. S28b†), in agreement with the theoretical calculations (2.41–2.56 eV). MOM **1** also shows emission maxima at *ca.* 432 nm and *ca.* 368 nm due to π–π interactions (Fig. S29†).

The electrical conductivity of MOM **1** has been measured for up to four different single crystals using the two-probe method (Fig. S30†) along the crystallographic *b*-axis. The electrical conductivity values for the four different crystals at 400 K are $1.7(1) \times 10^{-8}$, $4.0(1) \times 10^{-8}$, $1.8(1) \times 10^{-8}$ and $1.4(1) \times 10^{-7}$ S cm^{-1} (Fig. S31 and Table S7†). These measurements show a semiconducting behaviour in all cases with electrical conductivity values at 400 K in the range 10^{-7} to 10^{-8} S cm^{-1}, with an average value of $5(3) \times 10^{-8}$ S cm^{-1} (Fig. 4 and Table S7†). The thermal variation of the electrical conductivity shows a semiconducting behaviour in the range 360–400 K with an activation energy of 1.1–1.2 eV (Fig. 4b, S31b and Table S7†). The electrical conductivity can be attributed to the electron delocalization promoted by the π–π interactions of the supramolecular network.

Electrocatalytic oxygen reduction reaction (ORR) activity of MOM $[Cu(INA)_2(H_2O)_4]$ (1)

Controlling product selectivity in ORR is an outstanding challenge. While O_2 reduction to H_2O is thermodynamically favourable, O_2 reduction to H_2O_2 is kinetically favoured. Thus, O_2 reduction mostly affords H_2O_2. For fuel cell applications, O_2 reduction to H_2O is desirable and thus there is an ongoing effort to find efficient electrocatalysts for selective ORR to water. The ORR activity of MOM **1** was checked in alkaline solution (pH = 13). The number of electrons and the amount of H_2O_2 produced during the reaction were analysed using rotating ring disk electrode (RRDE). The ring potential was held at 0.1 V to oxidize the generated H_2O_2 while maintaining the rotation speed at 300 and 600 rpm. The onset potential for ORR was observed around 0.6 V for both, catalyst and blank electrodes (Fig. 5 and S32†). The current generated at the glassy carbon disk electrode for the catalyst was higher than that of the blank electrode while the generated ring current was higher for the blank electrode (Fig. 5 and S32†). These results indicate that the amount of H_2O_2 formed for the catalyst is lower than that of the blank electrode. Thus, the amount of H_2O_2 calculated for the catalyst was 18% and 30%, whereas for the blank electrodes, it was 61% and 55% at 300 and 600 rpm, respectively. The number of electrons transferred to the substrate for the catalyst and blank electrodes are 3.6 and 2.7, respectively. Therefore, the presence of the catalyst increases the H_2O/H_2O_2 ratio from 0.64 to 4.56 at 300 rpm. This results clearly demonstrate that the catalyst is more than seven times more selective towards water formation by catalysing the $4e^-/4H^+$ reduction of oxygen.

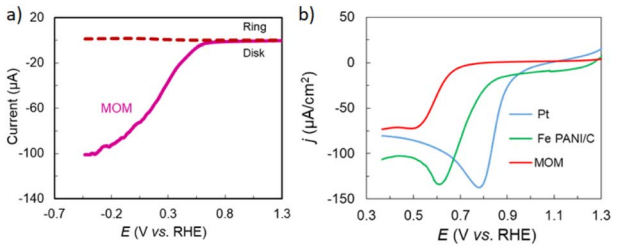

Fig. 5 (a) Rotating ring disk electrochemistry (RRDE) plots for the ORR of MOM **1** at pH = 13 and 300 rpm. Solid and dashed lines are the disk and ring currents, respectively. (b) Electrocatalytic ORR activity of MOM, Pt, and Fe PANI/C in air-saturated 0.1 M KOH. Experimental conditions: Pt wire and Ag/AgCl were used as the counter and reference electrodes, respectively.

For ORR in PEMFC, Pt/C is the commercial benchmark catalyst used in acidic medium.[48] Here the catalyst MOM **1** was compared with a 2 mm diameter Pt working electrode and with Fe PANI/C, one of the well-known non-noble metal catalysts reported for ORR.[49] The ORR was performed under air-saturated conditions in 0.1 M KOH solution (pH 13). The peak current observed for Pt, Fe PANI/C and MOM were 137, 134, and 45 μA, respectively. The onset potentials of ORR for Pt, Fe PANI/C and MOM are 0.96, 0.85 and 0.70 V *vs.* RHE, respectively (Table S8†).

We have recorded chronoamperometry data to check the stability of the material with carbon cloth (0.5×0.5 cm^2) (Fig. S33†). The electrolysis, performed at 0.56 V *vs.* RHE under O_2 saturated condition, shows a current density of −1.3 mA cm^{-2}, much higher than that of the blank carbon cloth current density obtained at the same potential. The material was

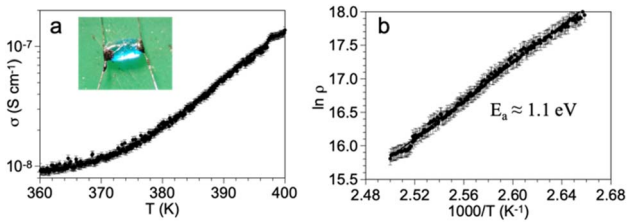

Fig. 4 (a) Thermal variation of the electrical conductivity of MOM **1**. Inset shows a picture of one of the single crystals used for the measurements. (b) Arrhenius plot of MOM **1** in the temperature range 400–375 K.

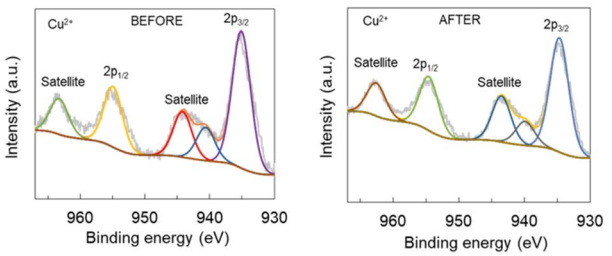

Fig. 6 XPS data of MOM **1**: before (left) and after (right) the electrolysis experiments.

Open Access Article. Published on 30 April 2025. Downloaded on 3/29/2026 5:07:54 PM. This article is licensed under a Creative Commons Attribution-NonCommercial 3.0 Unported Licence.

characterized using X-ray photoelectron spectroscopy (XPS) before and after electrolysis (Fig. 6). As can be seen in Fig. 6, the spectra are very similar and show the presence of Cu 2p peaks before and after electrolysis. In the XPS spectra before the electrolysis, the peaks centred at 935.1 eV and 954.9 eV correspond to $2p_{3/2}$ and $2p_{1/2}$, respectively. The satellite peaks were observed at 944.2 and 963.2 eV. These peaks indicate the presence of Cu^{2+} in agreement with the literature.[50–52] After the electrolysis, the $2p_{3/2}$ and $2p_{1/2}$ peaks appear at 934.6 and 954.5 eV, respectively. The satellite peaks appear at binding energies of 943.4 and 962.5 eV. Therefore, we can conclude that the material remains stable and did not decompose during the electrochemical reaction.

Conclusions

In conclusion, we have demonstrated the electrocatalytic ORR activity of a chemically stable dual conducting material for the first time. This compound, formulated as $[Cu(INA)_2(H_2O)_4]$ (**1**), shows a moderate proton conductivity of 2.26×10^{-5} S cm^{-1} at 298 K and 98% RH and an electrical conductivity of up to 10^{-7} S cm^{-1} at 400 K with a semiconducting behaviour and an activation energy of 1.1(1) eV. Compound **1** also shows a weak antiferromagnetic coupling mediated by strong π–π and H-bond interactions. Both, electron and proton transport, are supported by theoretical calculations. The electrocatalytic ORR study reveals that this dual-conducting material reduces oxygen selectively to water in alkaline conditions. We hope that this work will boost the systematic development of new dual conducting electrocatalysts.

Experimental

Physicochemical characterization of $[Cu(INA)_2(H_2O)_4]$ (1)

All the chemicals were of analytical grade and used as received without further purification. Elemental analyses (C, H and N) were performed using a PerkinElmer 240C elemental analyzer. The FTIR spectrum was measured on a Nicolet Impact 410 spectrometer between 400 and 4000 cm^{-1}, using KBr pellets. Absorption spectra were recorded on a UV/vis/NIR PerkinElmer Lambda 1050 spectrophotometer. Photoluminescence (PL) spectrum was recorded on a FLS1000 photoluminescence spectrometer (Edinburgh Instruments) equipped with a 450 W ozone free continuous xenon arc lamp and a photomultiplier (PMT-980) detector. Elemental mapping was carried out with AzTec INCA software. The thermal analysis was carried out using a Mettler Toledo TG-DTA 85 thermal analyser under a flow of N_2 (30 mL min^{-1}). The sample was heated at a rate of 10 °C min^{-1} with inert alumina as a reference. The powder X-ray diffraction (PXRD) data were collected using Empyrean PANalytical powder diffractometer with CuKα radiation ($\lambda = 1.54056$ Å). FESEM images were collected by using the field emission scanning electron microscope (FESEM) SCIOS 2 FIB-SEM and the corresponding EDX microanalysis was done by Oxford Ultim Max 170 Detector. Magnetic measurements were performed with a Quantum Design MPMS-XL-5 SQUID magnetometer in the 2–300 K temperature range with an applied magnetic field of 0.1 T on a polycrystalline sample of MOM **1** (with a mass of 25.126 mg). Susceptibility data were corrected for the sample holder and for the diamagnetic contribution of the salts using Pascal's constants.[53]

Synthesis of $[Cu(INA)_2(H_2O)_4]$ (1)

Single crystals of $[Cu(INA)_2(H_2O)_4]$ (**1**) were synthesized by carefully layering a 2 : 3 H_2O : MeOH (v/v) solution (3 mL) containing sodium isonicotinate (NaINA, 292.2 mg, 2 mmol) over an aqueous solution (3 mL) of copper(II) nitrate trihydrate (240.6 mg, 1 mmol). Sky blue elongated prismatic single crystals, suitable for X-ray diffraction (Fig. S34†) were grown at the interface of the two layers after three days. Yield: 60%. MOM **1** was also prepared as a bulk polycrystalline sample (Fig. S35†) by simply mixing aqueous solutions (3 mL) of sodium isonicotinate (292.2 mg, 2 mmol) with copper(II) nitrate trihydrate (240.6 mg, 1 mmol) in a 2 : 1 ratio. Yield: 90%. Elemental analysis: Anal. cald: $C_{12}H_{16}CuN_2O_8$: C, 37.95; H, 4.25; N, 7.38%. Found: C, 37.79; H, 4.11; N, 7.28%. Details of the crystallographic data collection and crystal structure resolution can be found in the ESI.†

Data availability

The data supporting this article have been included as part of the ESI.† These data include: details of the experimental measurements, PXRD, single-crystal structure analysis (including tables with the crystal data, Table S2,† bond distances and angles, Table S3,† structural parameters of the H-bonds, Table S4,† and π–π and anion–π interactions, Table S5†), Hirshfeld surface analysis, theoretical calculation details, stability tests details, water adsorption study, band structure calculation, electrical and proton conductivity measurements, rotating ring disk electrode (RRDE) analysis and details of the preparation of the electrodes. Table S1† includes electrical and proton conductivity values and applications of the all the reported dual conductors. The CIF for the structure reported in this article has been deposited at the Cambridge Crystallographic Data Centre (CCDC) under deposition number CCDC 2369691.† These data can be obtained free of charge from the CCDC *via* **https://www.ccdc.cam.ac.uk/structures**. All relevant data supporting the findings of this study are available from the corresponding authors on request.

Author contributions

Conceptualization: R. S. and C. J. G. G.; data curation and formal analysis: all authors; funding acquisition: C. J. G. G., M. L. S. and A. F.; methodology: R. S., A. S., A. I. S., B. M., M. S. L., S. B., A. F. and C. J. G. G.; investigation: R. S., A. S., A. I. S., B. M., M. S. L., S. B., A. F. and C. J. G. G.; writing – review & editing: all authors; supervision: R. S., M. S. L. and C. J. G. G.

Conflicts of interest

There are no conflicts to declare.

 © 2025 The Author(s). Published by the Royal Society of Chemistry

Open Access Article. Published on 30 April 2025. Downloaded on 3/29/2026 5:07:54 PM.
This article is licensed under a Creative Commons Attribution-NonCommercial 3.0 Unported Licence.

Acknowledgements

R. S. is beneficiary of the grant (Z21-070) for the requalification of the Spanish University system from the Ministry of Universities of the Government of Spain, modality "María Zambrano" financed by the European Union. This study forms part of the Advanced Materials program and was supported by the Spanish MCIN with funding from European Union Next Generation EU (PRTR-C17.I1) and the Generalitat Valenciana (project MFA-2022-057). We also thank the Grants PID2021-125907NB-I00 and TED2021-130946B-100 funded by MCIN/AEI/10.13039/501100011033 and by "ERDF A way of making Europe" and project CIPROM-2022-060 from the Generalitat Valenciana, for financial support. M. S. L. thanks the grant 2022R1A2C2005339 funded by the National Research Foundation (NRF) of Korea.

Notes and references

1 M. T. Koper, *Chem. Sci.*, 2013, **4**, 2710–2723.
2 D. G. Nocera, *J. Am. Chem. Soc.*, 2022, **144**, 1069–1081.
3 D. R. Weinberg, C. J. Gagliardi, J. F. Hull, C. F. Murphy, C. A. Kent, B. C. Westlake, A. Paul, D. H. Ess, D. G. McCafferty and T. J. Meyer, *Chem. Rev.*, 2012, **112**, 4016–4093.
4 R. E. Warburton, A. V. Soudackov and S. Hammes-Schiffer, *Chem. Rev.*, 2022, **122**, 10599–10650.
5 S. R. Hui and P. De Luna, *Matter*, 2021, **4**, 1555–1577.
6 J. Luo, X. Jia and C. Ren, *Matter*, 2022, **5**, 772–774.
7 S. Yang, J. Han and W. Zhang, *Chem.–Eur. J.*, 2023, **29**, e202302770.
8 E. Fabbri, D. Pergolesi and E. Traversa, *Chem. Soc. Rev.*, 2010, **39**, 4355–4369.
9 L. Cao, H. Wu, Z. Mu, X. He, C. Wang, J. Li, Y. Li, M. Xu and Z. Jiang, *J. Mater. Chem. A*, 2018, **6**, 8499–8506.
10 J. Wind, R. A. Mole, D. Yu, M. Avdeev and C. D. Ling, *Chem. Mater.*, 2018, **30**, 4949–4958.
11 K. Hatakeyama, H. Tateishi, T. Taniguchi, M. Koinuma, T. Kida, S. Hayami, H. Yokoi and Y. Matsumoto, *Chem. Mater.*, 2014, **26**, 5598–5604.
12 T. R. Cook, Y. Zheng and P. J. Stang, *Chem. Rev.*, 2012, **113**, 734–777.
13 M. D. Allendorf, R. Dong, X. Feng, S. Kaskel, D. Matoga and V. Stavila, *Chem. Rev.*, 2020, **120**, 8581–8640.
14 A. Sharma, J. Lim and M. S. Lah, *Coord. Chem. Rev.*, 2023, **479**, 214995.
15 R. Saha, K. Gupta and C. J. Gómez García, *Cryst. Growth Des.*, 2024, **24**, 2235–2265.
16 Y. Liu, Y. Chen, Q. Zhuang and G. Li, *Coord. Chem. Rev.*, 2022, **471**, 214740.
17 J. Su, W. He, X. Li, L. Sun, H. Wang, Y. Lan, M. Ding and J. Zuo, *Matter*, 2020, **2**, 711–722.
18 Y. Zou, T. Zhan, Y. Yang, Z. Fan, Y. Li, Y. Zhang, X. Ma, Q. Chen, S. Xiang and Z. Zhang, *J. Mater. Chem. A*, 2022, **10**, 3216–3225.
19 M. Donoshita, Y. Yoshida, M. Maesato and H. Kitagawa, *J. Am. Chem. Soc.*, 2022, **144**, 17149–17155.
20 X. He, B. Shao, R. Huang, M. Dong, Y. Tong, Y. Luo, T. Meng, F. Yang, Z. Zhang and J. Huang, *Adv. Sci.*, 2023, **10**, 2205944.
21 J. Y. Choi, M. Stodolka, N. Kim, H. T. Pham, B. Check and J. Park, *Chem*, 2023, **9**, 143–153.
22 M. Park, H. Ju, J. Oh, K. Park, H. Lim, S. M. Yoon and I. Song, *Nat. Commun.*, 2025, **16**, 1316.
23 C. Ribeiro, B. Tan, F. Figueira, R. F. Mendes, J. Calbo, G. Valente, P. Escamilla, F. A. A. Paz, J. Rocha, M. Dincă and M. Souto, *J. Am. Chem. Soc.*, 2025, **147**, 63–68.
24 P.-H. Wang, Y. Yoshida, S. Yasaka, M. Maesato, Y. Nakano and H. Kitagawa, *J. Am. Chem. Soc.*, 2025, **147**, 3804–3812.
25 R. Bashiri, P. S. Lawson, S. He, S. Nanayakkara, K. Kim, N. S. Barnett, V. Stavila, F. E. Gabaly, J. Lee, E. Ayars and M. C. So, *Chem. Mater.*, 2025, **37**, 1143–1153.
26 Y.-M. Jo, D.-H. Kim, J. Wang, J. J. Oppenheim and M. Dinca, *J. Am. Chem. Soc.*, 2024, **146**, 20213–20220.
27 N. Zion, A. Friedman, N. Levy and L. Elbaz, *Adv. Mater.*, 2018, **30**, 1800406.
28 S. Chatterjee, K. Sengupta, B. Mondal, S. Dey and A. Dey, *Acc. Chem. Res.*, 2017, **50**, 1744–1753.
29 M. Shao, Q. Chang, J. Dodelet and R. Chenitz, *Chem. Rev.*, 2016, **116**, 3594–3657.
30 R. P. Gautam, Y. T. Lee, G. L. Herman, C. M. Moreno, E. C. Tse and C. J. Barile, *Angew. Chem., Int. Ed.*, 2018, **130**, 13668–13671.
31 X. F. Lu, B. Y. Xia, S. Zang and X. W. Lou, *Angew. Chem., Int. Ed.*, 2020, **132**, 4662–4678.
32 X. Huang, L. Gan, J. Wang, S. Ali, C. He and H. Xu, *J. Phys. Chem. Lett.*, 2021, **12**, 9197–9204.
33 M. Zhang, Q. Lin, W. Wu, Y. Ye, Z. Yao, X. Ma, S. Xiang and Z. Zhang, *ACS Appl. Mater. Interfaces*, 2020, **12**, 16367–16375.
34 J. Chen, B. An, Y. Chen, X. Han, Q. Mei, M. He, Y. Cheng, I. J. Vitorica-Yrezabal, L. S. Natrajan and D. Lee, *J. Am. Chem. Soc.*, 2023, **145**, 19225–19231.
35 K. Waizump, M. Takuno, N. Fukushima and H. Masuda, *J. Coord. Chem.*, 1998, **44**, 269–279.
36 C. Z. Lin, S. S. Chui, S. M. Lo, F. L. Shek, M. Wu, K. Suwinska, J. Lipkowski and I. D. Williams, *Chem. Commun.*, 2002, 1642–1643.
37 N. Okabe, T. Nakamura and H. Fukuda, *Acta Crystallogr., Sect. C:Struct. Chem.*, 1993, **49**, 1761–1762.
38 M. Cao, J. Wu, J. Liang and B. Ye, *Cryst. Growth Des.*, 2010, **10**, 4934–4942.
39 M. Almáši, Z. Vargová, R. Gyepes, R. Varga and V. Zeleňák, *Inorg. Chem. Commun.*, 2014, **46**, 118–121.
40 L. Wang, T. Zeng, G. Liao, Q. Cheng and Z. Pan, *Polyhedron*, 2019, **157**, 152–162.
41 Y. Liu, A. Yang, X. Zhang, Z. Sun, W. Li, Y. Wang, J. Luan and H. Liu, *J. Environ. Chem. Eng.*, 2022, **10**, 108215.
42 B. K. Das, S. J. Bora, M. Chakrabortty, L. Kalita, R. Chakrabarty and R. Barman, *J. Chem. Sci.*, 2006, **118**, 487–494.
43 D. B. Brown, J. A. Donner, J. W. Hall, S. R. Wilson, R. B. Wilson, D. J. Hodgson and W. E. Hatfield, *Inorg. Chem.*, 1979, **18**, 2635–2641.
44 R. D. Willett, C. J. Gómez-García, B. Twamley, S. Gómez-Coca and E. Ruiz, *Inorg. Chem.*, 2012, **51**, 5487–5493.

Open Access Article. Published on 30 April 2025. Downloaded on 3/29/2026 5:07:54 PM.
This article is licensed under a Creative Commons Attribution-NonCommercial 3.0 Unported Licence.

45 Y. N. Shvachko, D. V. Starichenko, A. V. Korolev, D. W. Boukhvalov and V. V. Ustinov, *Solid State Commun.*, 2009, **149**, 2189–2193.
46 P. Ramaswamy, N. E. Wong and G. K. Shimizu, *Chem. Soc. Rev.*, 2014, **43**, 5913–5932.
47 D. Lim, M. Sadakiyo and H. Kitagawa, *Chem. Sci.*, 2019, **10**, 16–33.
48 H. Cruz-Martínez, P. T. Matadamas-Ortiz, J. C. Ortiz-Herrera, E. López-Chávez, O. Solorza-Feria and D. I. Medina, *Mater. Today Phys.*, 2021, **19**, 100406.
49 S. Behera, S. T. Aziz, N. Singla and B. Mondal, *Chem. Commun.*, 2023, **59**, 11528–11531.
50 W. Cheng, Z. P. Wu, D. Luan, S. Q. Zang and X. W. Lou, *Angew. Chem., Int. Ed.*, 2021, **50**, 26601–26606.
51 D. A. Bulushev, A. L. Chuvilin, V. I. Sobolev, S. G. Stolyarova, Y. V. Shubin, I. P. Asanov, A. V. Ishchenko, G. Magnani, M. Riccò, A. V. Okotrub and L. G. Bulusheva, *J. Mater. Chem. A*, 2017, **5**, 10574–10583.
52 S. Cheng, T. Shi, X. Tao, Y. Zhong, Y. Huang, J. Li, G. Liao and Z. Tang, *Electrochim. Acta*, 2016, **212**, 492–499.
53 (*a*) G. A. Bain and J. F. Berry, *J. Chem. Educ.*, 2008, **85**, 532–536; (*b*) M. T. Koper, *Chem. Sci.*, 2013, **4**, 2710–2723.

 © 2025 The Author(s). Published by the Royal Society of Chemistry